SSC13-VIII-5

Design of Nano-satellite Cluster Formations for Bi-Directional Reflectance Distribution Function (BRDF) Estimations

Sreeja Nag
Massachusetts Institute of Technology
77 Massachusetts Avenue, Cambridge, MA 02139; 617-710-1845
sreeja_n@mit.edu

Faculty Advisor: Prof. Olivier de Weck
Massachusetts Institute of Technology

ABSTRACT

The bidirectional reflectance distribution function (BRDF) of the Earth's surface describes the directional and spectral variation of reflectance of a surface element. It is required for precise determination of important geophysical parameters such as albedo. BRDF can be estimated using reflectance data acquired at large 3D angular spread of solar illumination and detector directions and visible/near infrared (VNIR) spectral bands. This paper proposes and evaluates the use of nanosatellite clusters in formation flight to achieve large angular spreads for cheaper, faster and better estimations that will complement existing BRDF data products. In this paper, the technical feasibility of this concept is assessed in terms of various formation flight geometries available to achieve BRDF requirements and multiple tradespaces of solutions proposed at three levels of fidelity – Hill's equations, full sky spherical relative motion and global orbit propagation. Preliminary attitude control requirements, as constrained by cluster geometry, are shown to be achievable using CubeSat reaction wheels.

SCIENCE BACKGROUND

Multi-angle, multi-spectral remote sensing furnishes measurements of a very important target property called Bidirectional reflectance-distribution function (BRDF). BRDF of an optically thick body is a property of the surface material and its roughness, and depends on 3D geometry of incident and reflected elementary beams[1]. It is used in many earth science remote sensing applications, e.g. derivation of surface albedo, calculation of radiative forcing[2], land cover classification, cloud detection, atmospheric corrections, aerosol optical properties[3]. Local BRDF estimation is a 5 dimensional problem – 4 angular dimensions of incidence and reflectance (solar and detector, zenith and azimuth) and 1 spectral. To capture all the important optical features necessary for describing different surface types, a BRDF-oriented space mission[4] requires radiance measurements across a large angular spread of both solar illumination and detector directions, fine spatial resolution, frequent repeat of the ground track for a high temporal resolution and measurements across multiple wavelengths - large spectral range, high spectral resolution in the visible and near infrared (VNIR) solar spectrum (Table 1) and sometimes polarization state. Trade-offs between the variables depend on geoscience applications where the theoretical BRDF is used.

All **spaceborne** instruments (Table 1) provide sparse sampling of the BRDF function. These instruments estimate BRDF by making multi-angular measurements owing to their large cross track swath (e.g. Moderate Resolution Imaging Spectroradiometer-MODIS[5], Polarization and Directionality of the Earth's Reflectances-POLDER[6], Clouds and Earth's Radiant Energy System-CERES[7]), multiple forward and aft sensors (e.g. Multi-angle Imaging SpectroRadiometer-MISR[8], Along Track Scanning Radiometer-ATSR[9], Advanced Spaceborne Thermal Emission and Reflection Radiometer-ASTER[10]), or autonomous maneuverability to point at specific ground targets that they have been commanded to observe (e.g. Compact High Resolution Imaging Spectrometer -CHRIS[11]). But all the instruments fall short in at least one major BRDF science metric mentioned, highlighted with red in Table 1. POLDER, CERES have very coarse ground resolution, MISR, CERES have a small spectral range with very few bands and CHRIS has no target repeatability to capture BRDF change. Since BRDF sampling requires simultaneous reflectance measurements at multiple angles for a given ground footprint, one satellite is insufficient for accurate characterization (Figure 1). A single satellite can make measurements only along a restrictive plane with respect to the solar phase. Most EOS satellites are even more restricted since they are on sun-synchronous orbits. Further, the angular measurements are separated in time by many minutes along-track (e.g. MISR) or weeks cross-track (e.g. MODIS). In areas of fast changing surface/cloud conditions especially during the melt season/tropical storms, a few days can make a big difference in reflectance. Thus, all instruments that are dependent on large swaths have no angular range within a reasonable time-frame (marked N/A in Table 1), while those dependent on multiple sensors are limited by the sensor numbers. Finally, all the current BRDF instruments are nearing end of life and with the lack of a morning orbit in the JPSS-era, there will be a temporal gap in global BRDF measurements.

Airborne instruments can maximize fulfilling all science metrics except global coverage and repeatability; it is extremely expensive to scale up this shortcoming. NASA's heritage airborne BRDF instrument is called the Cloud Absorption Radiometer (CAR), developed at Goddard Space Flight Center (GSFC), has 14 channels of bandwidth 6-40 nm, makes up to 114600 directional measurements of radiance per channel per aircraft circle at a spatial resolution of 10-270 m but samples select geographic locations in few hours[3].

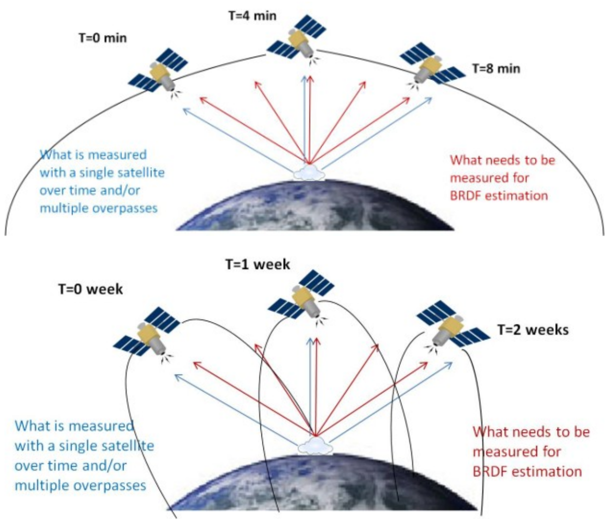

Figure 1: Measurements a single satellite is capable of making, in blue, versus measurements required for BRDF estimation, in red. 'T', ranging over a few minutes for fwd-aft sensors in the top panel or over a few weeks for cross-track sensors in the bottom panel, represents nominal time differences that a LEO satellite takes to make the given measurements.

Specific science applications govern the relative importance of Table 1's metrics. For example, up to 90% of the errors in the computation of atmospheric radiative forcing, which is a key assessor of climate change, is attributed to the lack of good angular description of reflected solar flux[12]. Aerosol retrievals are primarily affected due to lack of polarization data[8]. MODIS albedo retrievals show errors upto 15% due to its angular and spatial undersampling when compared to CAR. Gross Ecosystem Productivity (GEP) estimations (from CHRIS), to quantify sinks for anthropogenic CO_2, show uncertainties up to 40% because they need denser spatial, temporal reflectance measurements than CHRIS's angular data can provide[13]. Vegetation analysis is crippled due to severe under-sampling on the solar principal plane, and thus the backscattering hotspots[14].

Table 1: Comparison of current spaceborne mission instruments with BRDF products (rows) in terms of BRDF measurement metrics (columns). Dark red highlights indicate sparse measurements for BRDF estimation. The red box shows the measurement challenge that this paper will attempt to solve.

Science Metrics → Current Instruments ↓	Number of angles	Ground Pixel Size in km X km	Revisit Time (any view) in days	Spectral Range	# of spectral bands
[1]MODIS [1]	1	0.25 to 1	~2(16day RGT)	0.4-14.4 µm	36
[1]POLDER [2]	14	6 X 7	~2(16day RGT)	0.42-0.9 µm	9
[1]CERES [3]	1	10 to 20	~2(16day RGT)	0.3-12 µm	3
[2]MISR [4]	9	0.275 to 1.1	9(16 day RGT)	0.44-0.87 µm	4
[2]ATSR [5]	2	1 to 2	3-4	0.55–12 µm	7
[2]ASTER [6]	2	0.015 to 0.09	~2(16day RGT)	0.52–11.65 µm	14
[3]CHRIS [7]	5-15	0.17 to 0.5	As per command	0.415-1.05 µm	18-63

NANOSATELLITE CLUSTER FORMATIONS FOR SCIENCE

Full, global, repeatable sampling of the BRDF function is thus a big science challenge and this paper explores the possibility of addressing this challenge using distributed space systems (DSS). There are several buzzwords that have emerged with respect to the concept of using distributed spacecrafts i.e. physically separate modules for measurements. A **constellation** is defined as two or more spacecraft in similar orbits serving the same mission goal. A **cluster** is two or more spacecraft in a constellation that need to maintain relative positions and proximity to each other in orbit. They may need to use active control to maintain so or manipulate the orbits in such a way that some of their relative geometries are constant (closed form). Orbit corrections (for atmospheric drag, solar radiation pressure, non spherical earth and third body effects) will be needed even if closed solutions of the orbit equations are used to minimize active control to maintain specific geometries or schemes such as frozen orbits or sun-synchronous orbits are used. Clusters are said to fly in formation [15]. It is possible to have a constellation of clusters or a **clustellation**, where multiple clusters or localized groups of physically separate spacecraft fly in similar orbits like a constellation. Constellations of large satellites have been used in the past for earth observation, e.g. the A-

Train, GRACE and SWARM. MicroMAS, a microwave radiometer on a 3U CubeSat developed at MIT[17], is currently planned to be expanded from a single cubesat to a constellation of cubesats called "Dome". Aurora Flight Sciences is developing a system of fractionated spacecraft of cubesats called "MotherCube" that will triangulate radio-frequency sources on earth. **DSS and formation flight concepts** are currently gaining momentum in NASA after a decade of relative slack. The Earth Science Vision 2030, developed by ESTO, demonstrates its utility in Earth Science. Formation Flight has only been theoretically demonstrated in the past in the TechSAT program in SSL[18], J2 invariant orbit calculations[19], calculation of Keplerian orbits from the Hill's frame equations using differential COWPOKE equations[20] and quantifying cost and performance of DSS using systems engineering frameworks[21,22].

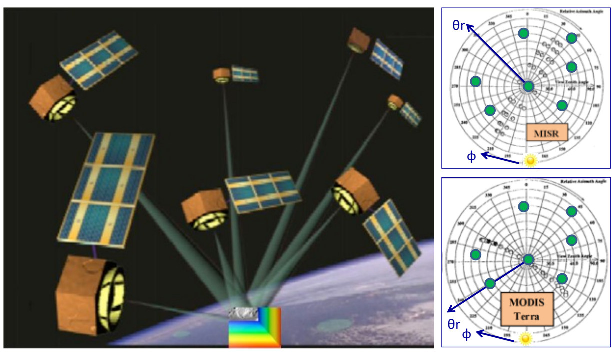

Figure 2: [Left] A DSS making multi-angular, multi-spectral measurements, as it orbits the Earth as a single system (adapted[2]). [Right] BRDF measurement plot in measurement zenith (ϴr) and relative azimuth (φ) for MODIS and MISR (black and white circles) on TERRA for [lat,long]=[0,0] over a 16-day period. The overlay of green dots indicate a hypothetical spread if a 7-satellite cluster, similar to the left panel, is used.

A DSS of nanosatellites (<10 kg) on a repeating-ground-track orbit appears to be an ideal solution to make BRDF-required reflectance measurements. DSS can make multi-spectral measurements of a ground spot at multiple 3D angles at the same time as they pass overhead (Figure 2 left panel). The right panel in Figure 2 shows the measurement spread as black and white circles for MISR (top) and MODIS (bottom), both on the same spacecraft TERRA, for the same target over a 16 day period. Each circle represents a measurement, taken at a specific azimuth from the sun (given by the polar azimuth of the plot) and at a specific zenith angle (given by the radius). The spread is not much even over a couple of weeks. The spread can be improved when the pictured DSS is used, as seen by the green circles in the figure – not to scale. Zenith and azimuthal coverage can be increased by increasing the number of satellites in a formation flight cluster and solar angle coverage can be increased by increasing the number of clusters (only one cluster shown in Figure 2) in a clustellation. Nanosatellites are a good choice for the DSS because many can be deployed for the mass and cost of a current large monolith. The 6U cubesat standard can be used, which is a standard satellite bus ideal for university programs and the largest satellites for launch on the Poly-PicoSatellite Orbital Deployer [23]. The GENSO (Global Educational Network for Satellite Operations) ground station network will make hundreds of data download centers available globally for frequent tracking and downlink. For adequate spatial and spectral sampling, small VNIR spectrometers can be configured for snapshot hyperspectral imaging.

To evaluate the performance of the proposed idea, we are building a systems engineering (SE) model integrated with traditional BRDF estimation models for tradespace exploration and optimization. The SE model will contain the following modules: global orbits and formation flight cluster geometry, attitude control systems, payload and complexity evaluation. The model will take BRDF measurement requirements and 6U cubesat/nanosatellite bus requirements as inputs, use them as constraints to generate hundreds of cluster architectures and output two types of metrics - science performance (e.g. Signal-to-Noise Ratio or SNR) and resource measures (e.g. mass). The model will also allow optimization within the individual modules to maximize metric values. Initial input measurement requirements come from science metric values of existing, successful spaceborne instruments (e.g. MISR, MODIS) and airborne (e.g. CAR) instrument data and include spatial resolution < 500 m, measurement Zenith Angles upto 60^o, measurement Azimuth upto 360^o, solar zenith Angles upto 80^o, more than14 spectral bands and spectral range between 350-2300 nm. Bus requirements come from 6U cubesat constraints (mass < 10 kg, volume < 10X20X30 cm, power < 25 W) and typical launch availabilities (Altitude between 400 and 800 km).

This paper focuses on the **global orbits and formation flight cluster geometry module** in the SE Model to improve the angular sampling of the BRDF function (red box in Table 1). This module takes some measurement requirements as inputs and checks all the cluster geometry solutions that satisfy them, in keeping with the sensor capabilities backpropagated from the ADCS module and the field of view capabilities from the payload model. The tradespace of cluster configurations possible for useful BRDF, required technologies and its implications on the other modules or effect on other figures of merit such as spatial resolution are presented.

FORMATION FLIGHT SOLUTIONS

This section uses insights from the above previous literature to identify cluster geometry solutions for the BRDF mission at three increasing levels of fidelity. At the first level we use the linearized Hill, Clohessy and Wiltshire equations, simplified to be known as the Hill's equations[24,25] to describe relative motion between any two spacecraft in a cluster, and can be extended to multiple spacecrafts. In this framework, one satellite is assumed to be traveling in a circular Keplerian orbit while the others are perturbed from this orbit by a small quantity compared to the height of the orbit. Since BRDF estimation requires inter-satellite zenith angles upto 80^o, very large inter-satellite distances are required which violate the assumptions of the HCW equation. Thus, while HCW solutions are a good approximation for trade studies, a higher level of fidelity is required for which we use parametric equations based on full-sky spherical geometry[26] for the relative motion among satellites, all in Keplerian orbits around an inertial Earth. Finally, to account for perturbations such as atmospheric drag, solar radiation pressure, non spherical earth and third body effects that accumulate over several orbits and need to be corrected for periodically, we use global modeling on Analytical Graphics Inc.'s Systems Tool Kit (AGI-STK[27]) i.e. the third and highest level of fidelity. Only a few cases from the HCW and the STK analysis will be shown.

Linearized Solutions using Hill Clohessy Wiltshire Equations

From the HCW Equations[24,25], 3D accelerations for any satellite with respect to the origin centered at the first satellite, X axis pointing radially away from the earth and Y axis in the direction of motion, is given by:

$$a_x = \ddot{x} - 3n^2x - 2n\dot{y}$$
$$a_y = \ddot{y} + 2n\dot{x}$$
$$a_z = \ddot{z} + n^2z \tag{1}$$

The additional orbit perturbations over and above these accelerations are J2 effects due to non-spherical Earth (typically 2.4 X 10^{-6} m/s^2 in LEO, differential acceleration being 4 orders smaller for a 1000m separation), third body perturbations due to differential force by the Sun and Moon on the spacecrafts (typically 3.6-4.3 X 10^{-5} m/s^2 in LEO, differential acceleration being 5 orders smaller), solar radiation pressure (typically 1.7X 10^{-10} m/s^2 in LEO and atmospheric drag due to small differences in the spacecraft shape and ballistic coefficient and atmospheric properties (typically 3.2X 10^{-9} m/s^2 in LEO). These accelerations need ΔV corrections which have not been discussed in this paper. By setting the acceleration terms in (1 to 0, we obtain the closed solutions to the Hill's equations i.e. relative geometries which do not need any active control to keep them intact. The analytical closed solution takes the following form [28] with 6 initial conditions:

$$x(t) = \frac{\dot{x}_0}{n}\sin nt - \frac{3x_0 + 2\dot{y}_0}{n}\cos nt + 4x_0 + \frac{2\dot{y}_0}{n}$$
$$y(t) = \frac{2\dot{x}_0}{n}\cos nt + \frac{6x_0 + 4\dot{y}_0}{n}\sin nt - (6nx_0 + 3\dot{y}_0)t - \frac{2\dot{x}_0}{n} + y_0$$
$$z(t) = \frac{\dot{z}_0}{n}\sin nt + z_0\cos nt \tag{2}$$

It can be seen that the x (zenith nadir) and y (along track) motions are coupled but the cross track/z motion is decoupled from both – elliptical motion. To avoid secular growth in relative motion, we can set the secular term to zero ($6nx_0 + 3\dot{y}_0 = 0$) in the second equation of (2. The other 5 initial conditions may be tweaked to produce the kind of relative motion desired. For example the offset in y (y_0) can be tweaked to produce an in plane formation of a train of satellites like the A-Train [29]. Discussed below are some closed solutions which can be used to make multi-angular BRDF measurements, obtained by closed form solutions of the Hill's equations i.e. no active contril needed to maintain relative configuration in the absence of perturbing natural disturbances. While those presented serve as representative examples, by changing the defining parameters in each configuration, a very large number of architectures are possible.

1. String of Pearls (SOP)

In this configuration, the satellites remain in a string in the along-track direction separated by a constant distance, say S km. The relative equations of motion for the k'th satellite are given by: $x_k(t) = 0$, $y_k(t) = kS$ and $z_k(t) = 0$. The string of pearls (SOP) cluster formation can recreate MISR-like measurements because it is possible to position 9 nanosatellites that are looking at the same ground spot at the same zenith angles that MISR looks at sequentially i.e. {-70.5 ; -60.0 ; -45.6 ; - 26.1000 ; 0 ; 26.1000 ; 45.6000 ; 60.0000 ; 70.5000}[8].While this configuration increases the chances of plume impingement, it reduces the chances of line of sight obstruction. It is the simplest solution for the HCW equations for multiple satellites.

2. Cross Track Scan

Since the X and Y motion in the HCW frame are uncoupled from the Z motion, the SOP configuration can be extended to include oscillations in the Z direction of any amplitude and phase desired. The frequency will be at the orbital angular rate. The relative equations of motion for the k'th satellite are given by: $x_k(t) = 0$, $y_k(t) = kS$ and $z_k(t) = z_0\cos(nt + \emptyset)$. z_0 and $\emptyset$ can be adjusted for any amplitude and phase, as per BRDF requirements or collision avoidance. For example, $\emptyset = (-1)^k\pi$ will case the satellites to oscillate 180 degrees out of phase with each other and minimize the risk of collision among consecutive tracks. Figure 3 shows a cross track scan configuration for a cluster of 5 satellites that project the following boresight angles to target when positioned along the orbit, i.e. along the Y-axis : -20°, 0°, 20°, 40°, 60°. All the satellites point their sensors toward the nadir spot on the ground (orange star) located at (0,0,-h) in the HCW frame where h is the orbit altitude. Note that the zenith angles with respect to nadir at the satellite, i.e. boresight angles, are ***smaller*** than the corresponding angles that the satellite subtends at the orange star with respect to zenith, i.e. view zenith angles, due to Earth's curvature.

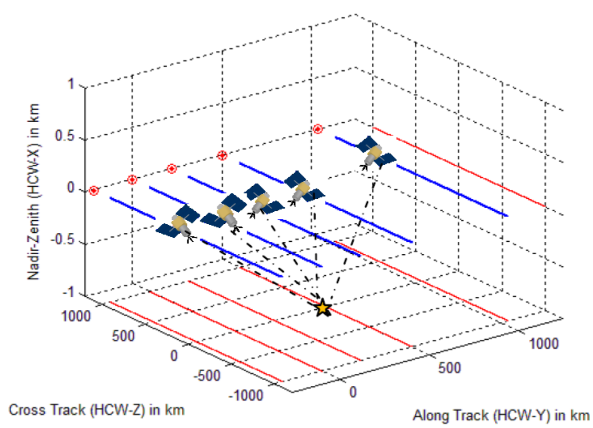

Figure 3: The Cross Track Scan configuration of a nanosatellite cluster (yellow and blue objects), their trajectories in the LVLH frame centered at (0,0,0) (blue lines) and the projections in 3 perpendicular planes (red lines/dots). The blue and yellow objects represent individual satellites, red dots represent the projection of their trajectories on each planes perpendicular to the 2 HCW axes. The nadir-zenith direction has been normalized [-1 1] and is not to scale, the orange star represents the target - point on the ground directly below the LVLH origin.

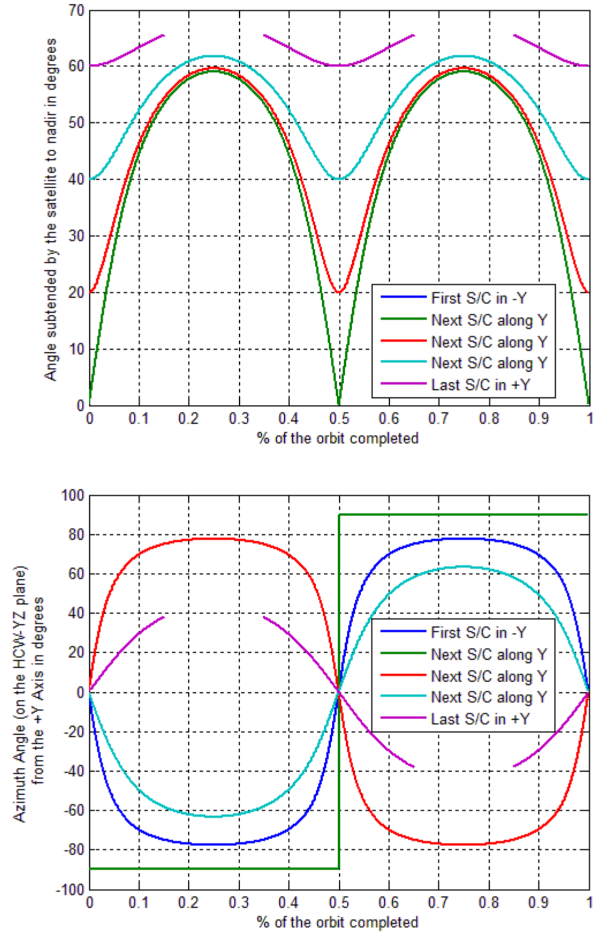

Figure 4: Variation of boresight or sensor viewing angle (top panel) at nadir (orange star in Figure 3 representing the target) and the azimuth (bottom panel) as measured on the YZ plane of the LVLH frame from +Y by the 5 satellites over one orbit for z_0 = 1000km and $\emptyset$= 0 for all. The leftmost satellite is called 'First S/C in -Y'.

As the satellites oscillate about the Y-axis, the boresight angle to the target (orange star in Figure 3) and the relative azimuth to the Y-axis changes periodically as seen in Figure 4, respectively for z_0 = 1000km and $\emptyset$= 0. Each satellite starts at the Y-axis, goes to one extreme then to the other extreme and then returns. Note that although z_0 and $\emptyset$ have been kept constant in the simulations shown, they can be varied to suit angles required. The azimuthal angle here in the LVLH or HCW frame is not the solar azimuth as shown on the BRDF plane – that would depend on the orientation of the orbit with respect to the sun in the global frame. The plots have been restricted to show angular variations for satellite lines of sight at >5° elevation, i.e. satellites considered only until 5° at the horizon, therefore restricting the maximum boresight angle that can be reached for line of sight (LOS) to nadir. In Figure 4, the purple curve representing the rightmost satellite in Figure 3-right panel, which subtends the maximum boresight angle among all, has been truncated at positions of the orbit where the satellites subtend the maximum boresight angle i.e. at z~ z_0. Figure 4-top panel has only four curves since the 1st (blue curve) and 3rd (red curve) satellite from the left have motions that are mirror images on the y=0 plane and this exactly same zenith motion and antisymmetric azimuthal motion (Figure 4-bottom panel). The green curve in Figure 4-bottom panel is a step function because it represents the 2nd satellite from the left whose motion is restricted to y=0 from where the azimuth is measured.

3. Free Orbit Ellipse (FOE)

The free orbit ellipse configuration has all the satellites arranged in elliptical rings around the LVLH origin. This configuration allows us to achieve both circular rings (at an angle of +/-26.565° to the horizontal) as well as elliptical rings that have circular projections on the ground/x=0 plane (at an angle of +/-30° to the horizontal) [28]. This configuration has been studied in great detail over the last decade to generate synthetic apertures using distributed space systems [18,15], a topic of interest to the US Air Force. For a ring formation that projects a circle on the ground [3028], the ellipse of relative motion must project a circle in the along track – cross track plane i.e. $y^2 + z^2 = r^2$, for a projected circle of radius r must always hold. If the initial conditions in (2 are chosen such that: $\dot{y_0} = -2nx_0$, $y_0 = 2\dot{x_0}/n$, $z_0 = \pm 2x_0$ and $\dot{z_0} = \pm 2\dot{x_0}$, then the Hill's Equations reduce to the following equations and a projected circle of radius as a function of initial x position and velocity only. It can be seen that the condition of the HCW equations that the x:y motion should always trace a 1:2 ellipse in the z=0 plane has been maintained. It is the mutual ratio with the z motion that has projected the circle. The corresponding ellipse has a semi major axis of length $\frac{\sqrt{5}}{2}$R where R is the radius of the projected circle. The relative equations of motion for the general; k'th satellite in an N-satellite cluster in the LVLH/HCW coordinate system are:

$$x(t) = \frac{\dot{x_0}}{n}\sin nt + x_0 \cos nt\,;\ x_k(t) = x_0 \cos\left(nt + \frac{2\pi k}{N} + t_0\right)$$

$$y(t) = \frac{2\dot{x_0}}{n}\cos nt - 2x_0 \sin nt\,;\ y_k(t) = -2x_0 \sin\left(nt + \frac{2\pi k}{N} + t_0\right)$$

$$z(t) = \frac{2\dot{x_0}}{n}\sin nt + 2x_0 \cos nt\ ;\ z_k(t) = z_0 \cos\left(nt + \frac{2\pi k}{N} + \emptyset_z\right) \quad \textbf{(3)}$$

Figure 5 shows the trajectories of 9 nanosatellites in free-elliptical orbits, 3 satellites per ring. The radii of the ellipses have been chosen such that their projected circles on the LVLH x=0 plane form following boresight angles when looking at nadir (orange star): 20°, 40°, 60°. For each ring, the phases have been chosen to be offset by 120°. The height of the orbit is at 600 km. (3 also shows that the phase of the Z motion is decoupled from X and Y, which gives us the liberty to phase out the 3 satellites as required. Similarly, many architectures are possible by changing the initial x_0/z_0 ratio which defines the angle of the HCW ellipse with the chief orbit and thus the shape of the ellipse. To quantify the effect of changing the initial conditions, a cluster of 6 satellites was simulated with an initial z_0 on the x=0 plane subtending a boresight angle of 40° at nadir (point on the ground directly below the HCW origin), x_0 = p$z_0$where p = {0.2;0.5;0.5774;1;2;3} and with zero initial phase for all. The cluster is an orbit of 600 km altitude. A big disadvantage of using this cluster is that the satellites tend to traverse enormous lengths in altitude, many of which will be unrealistic. For the plausible ones, the large variation will cause different satellites in the cluster to be at very different heights at different locations of the earth causing large differential drag that needs to be corrected for.

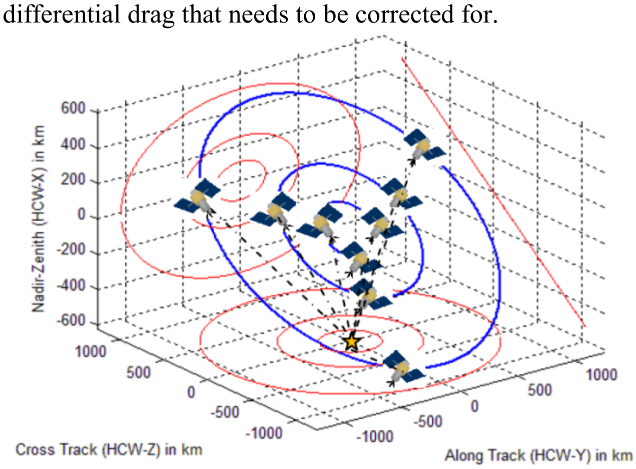

Figure 5: Free Orbit Ellipse configuration of a nanosatellite cluster (yellow and blue objects), their trajectories in the HCW frame centered at (0,0,0) (blue lines) and the projections in 3 perpendicular planes (red lines). The orange star represents the target – point on the ground directly below the LVLH origin. The dashed lines indicate the satellite line of sight (LOS) to target.

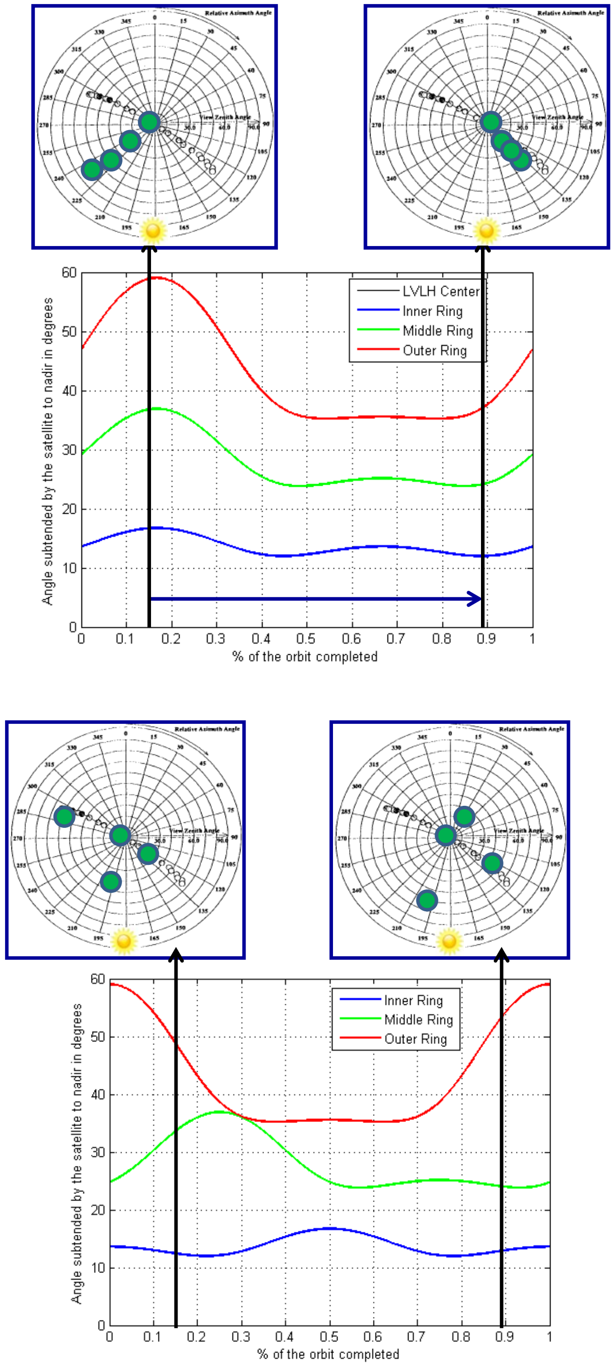

Figure 6: Variation of boresight or sensor viewing angle at nadir for an FOE cluster with $z_0 = 2.5x_0$, 3 rings, 1 satellite per ring and 1 satellite at the LVLH origin. The top panel has no phase difference between the satellites in each ring; the bottom panel has a 90^o phase difference. Polar plots of the measurement spread for two points in time have been drawn, top and bottom. The green dots are for the cluster while the black and white dots are simulated MODIS-TERRA measurements.

From the trades relating the ellipse size, shape and orientation to the chief orbit plane with the boresight and azimuthal angles, an example to show the implications of a candidate FOE cluster on the BRDF polar plot (e.g. right panel of Figure 2) was selected. Four satellites in 3 rings inclined at 21.8^o to the X=0 plane with one satellite in the center were simulated such that they projected boresight angles of 0^o, 15^o, 30^o, 45^o when crossing the LVLH Y-Axis. When the phase difference between the satellites was 0 (90^o), the boresight variation and BRDF polar plots for two points in time are shown in Figure 6 – top (bottom) panel assuming zero initial phase with the Sun. The curves show the variation of the boresight angle for the LOS to ground target for each of the satellites i.e. the sensor viewing angle in BRDF terms. This example shows that by tweaking the initialization of the HCW satellites, the relative phase and radii and the BRDF polar plot measurement spread can be customized and is capable of spreading out much more than the MODIS angular data.

Viewing Geometry for Satellite Relative Motion

This section calculates the area of the sensor footprint at the target for an assumed field of view (propagated from the payload module of the SE Model) by translating the interpretations from the LVLH frame to the Earth-centered frame in the following way. The nadir angle, η, is measured at the satellite from the subsatellite point in the nadir direction to the target point on the ground. The earth angle, λ, is measured at the Earth's center between the subsatellite point and target. The earth angular radius, ρ, is then given by:

$$\sin\rho = \cos\lambda_0 = \frac{R_E}{R_E + H} \tag{4}$$

Where R is the radius of the earth = 6378.1 km and H = altitude of the satellite. Next the relationship between the elevation angle, ε, the nadir angle, η, earth angular radius, ρ, and the earth central angle, λ, is given by:

$$\sin\eta = \cos\varepsilon\ \sin\rho$$
$$\lambda + \rho + \varepsilon = 90 \tag{5}$$

The distance to the target, D, and the distance to the true horizon, D_o, can then be found using:

$$\boldsymbol{D = R_E \frac{\sin\lambda}{\sin\eta}}$$
$$D_o = R_E / \tan\rho \tag{6}$$

From these derivations, it is obvious why the boresight angle subtended at the satellite between its line of sight to the target and the vertical, , i.e. η, is *smaller* than the view zenith angle subtended at the target between its line of sight to the satellite and the vertical, i.e. 90 - ε. Figure 4 and Figure 6 plotted the boresight vectors of the clusters. To get the corresponding view zenith angles in the BRDF plots, the above equations/map will be used. For analytical calculations of the sensor footprint at target [31], the length is measured in the boresight vector direction since it is expected to be longer and breadth in the perpendicular direction. The elevation angle, ε, is always measured at the toe of the footprint because that is where the performance is the worst. With an error in approximations (details in [31]) is proportionate to 1-($W_F/\sin(W_F)$), the footprint length, L_F, width, W_F and elliptical footprint area, F_A, is given by:

$$L_F = D \sin\theta / \sin\varepsilon$$
$$W_F = D \sin\theta$$
$$F_A = (\pi/4) L_F W_F$$

(7)

The importance of analyzing the footprint areas is that if satellites are looking at the same ground spot but with vastly different GREs, it is hard to combine the measurements into a single BRDF polar plot since the larger GRE will show much more spatial averaging of the ground anisotropy. Essentially, the objective of the cluster design should not only be appropriate angles at appropriate phases of the orbit but also that the GREs of the satellites are within a magnitude of each other.

Attitude Control Requirements for Satellite Relative Motion

Since there is significant variation of the angle subtended at nadir and azimuth by all the satellites in the clusters discussed, the satellites will need to constantly change their inertial initial attitude in order to point their payload toward the ground target. The orientation of a satellite in global space, in this case the LVLH frame, is defined by a 4D vector called a quaternion which maps the local coordinates of the satellite to the global coordinates and consists of a three-element hyper- imaginary vector part and a single-element scalar part: $\bar{q} = q_1\hat{\imath} + q_2\hat{\jmath} + q_3\hat{k} + q_4$, where the quantities $\hat{\imath}$, $\hat{\jmath}$, $\hat{k}$ follow a set of rules analogous to the single-dimension imaginary number $i = \sqrt{-1}$, and similar in form to the rules for forming cross products. The real coefficients of the quaternion components may be expressed in vector notation as $q = [q_1\ q_2\ q_3\ q_4]^T$. Given a rigid-body rotation of angle Θ about the axis, $\hat{n}$, expressed in some reference frame, the resulting orientation given by unit vector of the body may be characterized by:

$$q = \begin{bmatrix} q \\ q_4 \end{bmatrix} = \begin{bmatrix} \hat{n}\sin\left(\frac{\theta}{2}\right) \\ \cos\left(\frac{\theta}{2}\right) \end{bmatrix} = [q_1\ q_2\ q_3\ q_4]^T$$

(8)

Thus, a rotation of angle Θ about the unit vector $\hat{n}$, followed by a rotation of angle, Θ, about $\hat{n}$ results in zero change in attitude. In other words, the inverse of a quaternion may be found simply by changing the sign on the vector part. For simulating the attitude of our clusters, let us assume the instrument sensor for all the satellites are located on the –X face of the local body frame. When a satellite is at the origin of the LVLH from and pointing at nadir, the X-axis of the satellite and the X-axis of the LVLH frame are perfectly aligned. This position along with the corresponding Y and Z axes aligned is the normal quaternion for any of the satellites i.e. $[0\ 0\ 0\ 1]^T$ and it is the nominal imaging mode for a satellite at the LVLH origin. Satellites not at the origin have to tilt their line of sight (LOS) and therefore reorient from the normal quaternion in order to point their sensors to the LVLH nadir. If the satellite is located at an azimuth φ on the X=0 plane from the Y-axis and subtends an boresight viewing angle ψ at the LVLH nadir, then the new quaternion, as expressed in (8 with respect to the normal quaternion, is given by $\hat{n}$, i.e. [0 1 0] rotated about the X-axis by (φ - 90), and then ψ about $\hat{n}$.

$$\hat{n} = \begin{bmatrix} 1 & 0 & 0 \\ 0 & \cos(\Phi - 90) & -\sin(\Phi - 90) \\ 0 & \sin(\Phi - 90) & \cos(\Phi - 90) \end{bmatrix} \begin{bmatrix} 0 \\ 1 \\ 0 \end{bmatrix}$$
$$\hat{n} = \begin{bmatrix} 0 \\ \sin(\Phi) \\ -\cos(\Phi) \end{bmatrix}$$

(9)

The instantaneous quaternion for any satellite at an azimuth of φ (from +Y) and at a boresight angle of ψ from the LVLH nadir at any point of time in the cluster orbit can be given by:

$$q = \begin{bmatrix} q \\ q_4 \end{bmatrix} = \begin{bmatrix} \hat{n}\sin\left(\frac{\psi}{2}\right) \\ \cos\left(\frac{\psi}{2}\right) \end{bmatrix}$$
$$= \left[0\ \ \sin(\Phi)\sin\left(\frac{\psi}{2}\right)\ \ -\cos(\Phi)\sin\left(\frac{\psi}{2}\right)\ \ \cos\left(\frac{\psi}{2}\right)\right]^T$$

(10)

The quaternion associated with the body X axis of the satellite is zero without any loss of generality because the X-axis corresponds to the line of sight of the satellite sensor. The orientation about that axis is not of interest with respect to payload pointing. In the future as we design the solar panel or radiator orientation for the power or thermal systems respectively, q_1 will also be of interest and may need to be controlled. The required body angular rate, ω, can be found by differentiating the required quaternions in time (numerical first difference methods employed) and using (11 to solve for ω.

$$\dot{\bar{q}} = \frac{1}{2}\begin{bmatrix} q_x + q_4 I \\ -q^T \end{bmatrix}\omega = Q(\bar{q})\omega$$

Where

$$a = \begin{bmatrix} a_1 \\ a_2 \\ a_3 \end{bmatrix} => a^x = \begin{bmatrix} 0 & -a_3 & -a_2 \\ a_3 & 0 & -a_1 \\ -a_2 & a_1 & 0 \end{bmatrix}$$

(11)

The body angular rate and accelerations for all 4 satellites in the FOE cluster of Figure 6-top panel can be calculated using first differences to differentiate followed by the method above. The results for one orbit are shown in Figure 7. as expected, the outer ring shows maximum variation for all angular rates since it traces the largest ellipse. The first ~17% of the orbit and the last 33% in the figure, the satellites are at an altitude higher than the reference orbit i.e. the high end half of the ellipse, hence show lower variation of angles and angular velocities. The constrictions (bunching up) in the curves at two points in the orbit is because all the satellites cross the X=0 plane together at those points in time and lie in a circular projection, causing their instantaneous angular velocities (calculated based on their quaternion states alone) to be exactly equal. ω_y corresponds to body roll rate and ω_z to the body yaw rate, therefore are most affected by change in boresight and azimuth variation thus are the maximum.

Assuming the usual dimensions of a 10 kg 3U Cubesat and thus a moment of inertia to be 0.15 kg-m^2, commercially available reaction wheels are capable of supporting the required slew rate for all the satellites. For example, MAI-400 manufactured by Maryland Aerospace Inc. has a momentum storage capacity of 11.8 mNms and a torque authority of 0.625 mNm. Multiplying the body angular rate and acceleration in Figure 7 with the moment of inertia gives us a maximum required momentum storage capacity of 0.15 mNms and maximum torque of 2e-4 mNm in any axis, i.e. payload pointing requires <1% of the reaction wheel capacity. The rest is available for canceling disturbing torques. From the slew control point of view, we found that the FOE cluster outperforms the CTS cluster, although by a fractional margin given the total required maneuvers.

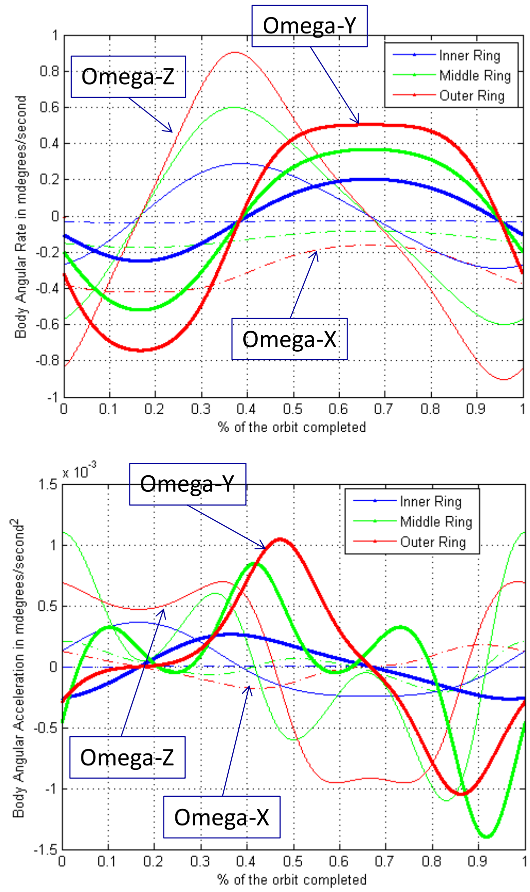

Figure 7: : Required body angular rates (top) and angular accelerations (bottom) of each satellite in the FOE cluster - Figure 6– to point its payload consistently at the LVLH origin's nadir point on the ground (orange star). The 3 rings are marked in different colors and ω_x (dashed line), ω_y (thin line), ω_z (thick line) in line types.

Relative Motion Solutions using Global Orbit Propagation

The HCW and full sky solutions do not take into account the global context of the clusters such as the solar orientation with time, rotating earth, geographic dependence of cluster geometry for real orbits, etc. or the secular and periodic disturbances such as J2 effects due to non-spherical Earth, differential atmospheric drag, solar radiation pressure, etc. These can be modeled using a global orbit modeling software to propagate the initial orbits over the mission lifetime. For this study, we used AGI's Systems Tool Kit (STK 10) – the basic version and Astrogator – along with Matlab R2011a. The following sections will present the preliminary results of the STK modeling as well as draw analogies with previous solutions to highlight the effect of the global disturbances and required corrections.

When satellites have the same semi-major axis (critical condition to hold the cluster) but differential Keplerian elements otherwise, the resultant relative motion is the FOE. To demonstrate a representative example, the orbits of three satellites with differential TA=0.2^o, 0.4^o, 0.6^o, inclinations = 29^o,30^o,31^o and differential eccentricities of 0.02, 0.04, 0.04 with respect to the reference satellite of inclination 28.5^o, TA=0^o, e=0 were propagated over one day and the resulting LVLH trajectories plotted in Figure 8. Functional combinations of the differential elements – inclination, eccentricity, RAAN, argument of perigiee and TA – therefore decide the FOE shape and orientation as analytically determined by the COWPOKE equations[20]. These parameters may be tweaked to produce many cluster geometry architectures. When the boresight angle subtended at the orange star for all the was plotted for the full day of orbit propagation, the effect of the ellipse drift on the subtended angle (a BRDF metric) is obvious from the change between the first orbit and the following ones. The extent and frequency to which this drift needs to be corrected depends on the specificity and revisit of the target required to be imaged.

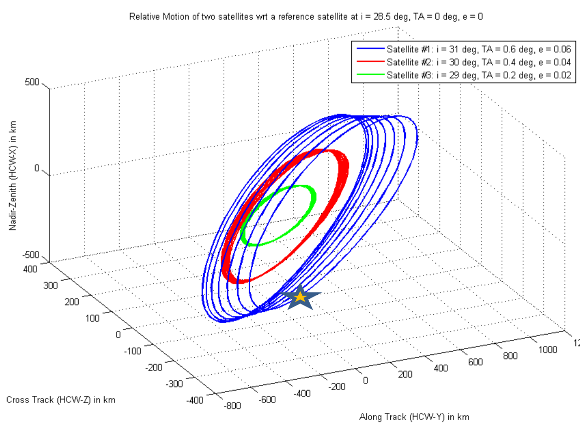

Figure 8: Orbits of 3 satellites with differential inclination, TA and eccentricity propagated using STK over a day's period and their trajectories plotted in the LVLH frame in blue, red and green. The orange star is point being imaged.

Using all the dependencies learned from the global STK trade studies above, a few candidate clusters with 9 satellites each (to match MISR's sensor numbers) were simulated to image a specific spot on earth [0, -103.729] – manrked as a yellow spot in Figure 9 amidst the cluster - at a repeat period of 16 days and compared to the measurement spread of the same ground spot by MISR. The Keplerian elements of all simulated satellites are listed in Table 2 and the corresponding BRDF plot of their simulated angular measurements of the target shown in Figure 10. Three clusters were simulated, one in the SOP configuration (black) with all Keplerian elements except the true anomaly the same and two others in different FOE configurations (blue and green). There was an approximate 60o between the chief orbit of MISR and any of the clusters. Due to MISR's large swath, it has ~1800s of access to the ground spot while the clusters have only 1.4 s in 16 days. Since MISR has fixed sensors, the measurement zenith angles for a direct overpass (plotted in pink) are pre-determined and the relative solar azimuth is the angle between the velocity and sun vector measured in the satellite HCW X=0 plane. These measurements for a single overpass can be replicated by an SOP cluster (plotted in black). The zenith angle is measured between the target to satellite vector and the zenith. The relative solar azimuth is measured between the target to satellite vector and the sun vector measured in the satellite HCW X=0 plane. The solar zenith angle is approximately ~89^o. The value of clusters is demonstrated in the FOE cluster examples where in a large and diverse azimuthal and zenith spread on the BRDF plot of possible by manipulating the initial Keplerian elements in Table 2.

Table 2: Initial Keplerian Elements for the Satellite Cluster Comparison Examples. "Satellite 1" is the reference satellite in each cluster and the corresponding chief orbit elements bolded

	a(km)	e	i (^{o})	Ω(^{o})	ω(^{o})	ν (^{o})
MISR	7075	0.00	98.3	138	122	280.79
SOP Cluster	7075	0.00	98.3	110	0.0	50:2.5:70
FOE Cluster #1						
Satellite1	**7075**	**0.0**	**98.3**	**110**	**0.0**	**285**
Satellite 2	7075	0.1	98.0	106	0.7	290
Satellite 3	7075	0.2	97.8	105	0.3	280
Satellite 4	7075	0.3	98.3	112	1.0	68.6
Satellite 5	7075	0.4	98.7	114	1.5	52.37
Satellite 6	7075	0.5	98.9	109	2.0	68.0
Satellite 7	7075	0.6	99.0	110	2.2	79.19
Satellite 8	7075	0.7	98.5	115	3.0	66.33
Satellite 9	7075	0.8	97.6	113	2.0	66.511
FOE Cluster #2						
Satellite1	**7075**	**0.00**	**98.3**	**110**	**0.0**	**59.232**
Satellite 2	7075	0.01	98.8	106	0.7	51.263
Satellite 3	7075	0.02	97.8	105	0.3	55.372
Satellite 4	7075	0.05	97.8	112	1.5	72.036
Satellite 5	7075	0.04	98.8	114	1.5	58.628
Satellite 6	7075	0.05	98.9	109	2.5	65.967
Satellite 7	7075	0.06	99.0	110	2.2	75.248
Satellite 8	7075	0.09	98.5	115	3.0	70.894
Satellite 9	7075	0.08	97.6	104	2.0	66.511

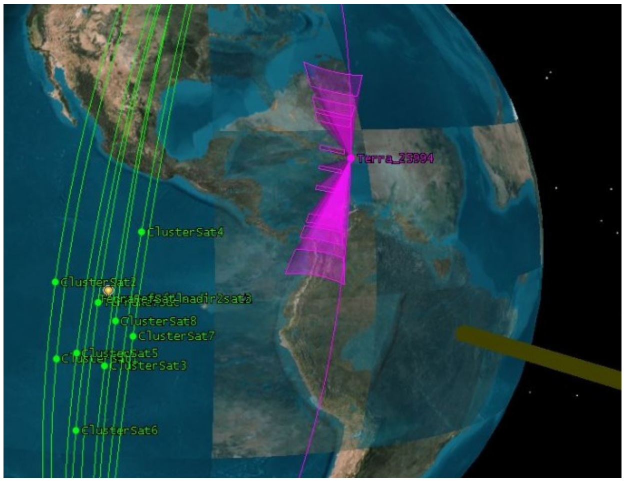

Figure 9: An STK global image of the TERRA spacecraft with its MISR instrument active – showing the field of view of its nine forward-aft cameras in pink – and a cluster of 9 satellites in green, both imaging a ground target marked in yellow (seen amidst the cluster). The yellow vector is pointing from the Earth to the Sun.

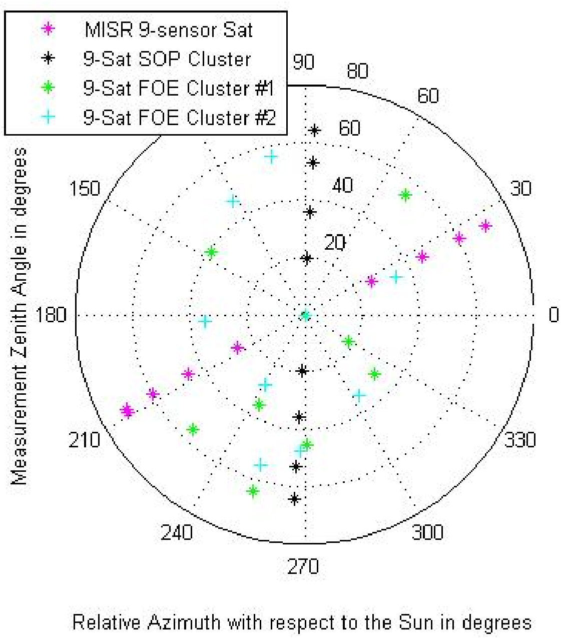

Figure 10: BRDF polar plot for STK simulated angular measurements (polar azimuth, radial zenith) for MISR and 3 candidate cluster architectures with 9 satellites each.

CONCLUSIONS

This paper proposes the use of nanosatellite clusters to achieve better angular (solar and sensor) sampling of the BRDF function of any ground spot than any of the current flight instruments provide. Several families of cluster configurations at different levels of fidelity and their effect in quantifying the BRDF angular spread have been described. By varying the key parameters, each family is capable of generating large numbers of cluster architectures. Representative examples have been demonstrated for achieving many boresight and azimuthal angles, view characteristics, attitude control and orbits. Finally, local and global examples have been compared to MODIS and MISR data to compare angular spread. For future work, the large architecture tradespace generated in this paper will be compared to each other as well as existing data products by inputting the angular spread into BRDF science models and calculating the BRDF estimation errors.

ACKNOWLEDGMENTS

I would like to thank Prof. Olivier de Weck at MIT and Charles Gatebe, Warren Wiscombe, Ralph Kahn, Jacqueline Lemoigne-Stewa, Miguel Roman and Conrad Schiff at NASA GSFC for very useful discussions on the topic of research presented.

REFERENCES

1. Nicodemus, F. E. *Geometrical considerations and nomenclature for reflectance*. 160, (US Department of Commerce, National Bureau of Standards Washington, D. C, 1977).
2. Esper, J., Neeck, S., Wiscombe, W., Ryschkewitsch, M. & Andary, J. Leonardo-BRDF: A New Generation Satellite Constellation. (2000).
3. Gatebe, C. K. Airborne spectral measurements of surface–atmosphere anisotropy for several surfaces and ecosystems over southern Africa. *Journal of Geophysical Research* 108, (2003).
4. Barnsley, M. J., Strahler, A. H., Morris, K. P. & Muller, J. P. Sampling the surface bidirectional reflectance distribution function (BRDF): 1. Evaluation of current and future satellite sensors. *Remote Sensing Reviews* 8, 271–311 (1994).
5. Xiong, X. *et al.* Terra and Aqua MODIS Design, Radiometry, and Geometry in Support of Land Remote Sensing. *Land Remote Sensing and Global Environmental Change* 133–164 (2011).
6. Deschamps, P. Y. *et al.* The POLDER mission: Instrument characteristics and scientific objectives. *Geoscience and Remote Sensing, IEEE Transactions on* 32, 598–615 (1994).
7. Wielicki, B. A. *et al.* Clouds and the Earth's Radiant Energy System (CERES): An earth observing system experiment. *Bulletin of the American Meteorological Society* 77, 853–868 (1996).

8. Diner, D. J. *et al.* Multi-angle Imaging SpectroRadiometer (MISR) instrument description and experiment overview. *Geoscience and Remote Sensing, IEEE Transactions on* 36, 1072–1087 (1998).
9. Godsalve, C. Bi-directional reflectance sampling by ATSR-2: a combined orbit and scan model. *Remote Sensing* 16, 269–300 (1995).
10. Abrams, M. The Advanced Spaceborne Thermal Emission and Reflection Radiometer (ASTER): data products for the high spatial resolution imager on NASA's Terra platform. *international Journal of Remote sensing* 21, 847–859 (2000).
11. Barducci, A., Guzzi, D., Marcoionni, P. & Pippi, I. CHRIS-Proba performance evaluation: signal-to-noise ratio, instrument efficiency and data quality from acquisitions over San Rossore (Italy) test site. in *Proceedings of the 3-rd ESA CHRIS/Proba Workshop, Italy* (2005).
12. Wielicki, B. A. & Harrison, E. F. Mission to planet Earth: Role of clouds and radiation in climate. *Bulletin of the American Meteorological Society* 76, (1995).
13. Hilker, T. *et al.* Inferring terrestrial photosynthetic light use efficiency of temperate ecosystems from space. *Journal of Geophysical Research: Biogeosciences* 116, n/a–n/a (2011).
14. Román, M. O. *et al.* Variability in surface BRDF at different spatial scales (30m–500m) over a mixed agricultural landscape as retrieved from airborne and satellite spectral measurements. *Remote Sensing of Environment* 115, 2184–2203 (2011).
15. Sedwick, R. J., Kong, E. M. C. & Miller, D. W. Exploiting orbital dynamics and micropropulsion for aperture synthesis using distributed satellite systems: Applications to Techsat 21. in *DCP Conf* (1998).at <http://www.aric.or.kr/treatise/journal/content.asp?idx=15425>
16. William Blackwell (1), Kerri Cahoy (2), David Miller (2), Idahosa Osaretin (1), and Annie Marinan (2) Nanosatellite for Earth Environmental Monitoring: The MICROMAS Project. 2012.B.2.4 Nanosatellite for Earth Environmental Monitoring, (2012).
17. Kong, E. M. C., Miller, D. W. & Sedwick, R. J. Exploiting orbital dynamics for aperture synthesis using distributed satellite systems- Applications to a visible Earth imager system. *Spaceflight mechanics 1999* 285–301 (1999).
18. Schaub, H. & Alfriend, K. T. J 2 invariant relative orbits for spacecraft formations. *Celestial Mechanics and Dynamical Astronomy* 79, 77–95 (2001).
19. Sabol, C., McLaughlin, C. & Luu, K. *The Cluster Orbits With Perturbations of Keplerian Elements (COWPOKE) Equations*. (DTIC Document, 2004).
20. Jilla, Cyrus D. A multiobjective, multidisciplinary design optimization methodology for the conceptual design of distributed satellite systems. (2002).
21. Shaw, G. B., Miller, D. & Hastings, D. E. Development of the Quantitative Generalized Information Network Analysis (GINA) Methodology for Satellite Systems. in *Aerospace Conference, 1999. Proceedings. 1999 IEEE* 5, 301–321 (1999).
22. Skrobot, G. & Coelho, R. ELaNa – Educational Launch of Nanosatellite: Providing Routine RideShare Opportunities. *AIAA/USU Conference on Small Satellites* (2012).
23. Hill, G. W. Researches in the lunar theory. *American Journal of Mathematics* **1**, 5–26 (1878).
24. W. H. Clohessy, R.S. Wiltshire Terminal Guidance System for Satellite Rendezvous. *Journal of Aerospace Science* **27**, 653–658 (1960).
25. Wertz, J. R. *Orbit & Constellation Design & Management, second printing ed. El Segundo*. (California: Microcosm Press, 2009).
26. Systems Tool Kit. *Analytical Graphics Inc.* at <http://www.agi.com/products/stk/modules/default.aspx/id/stk-free>
27. Sabol, C., Burns, R. & McLaughlin, C. A. Satellite formation flying design and evolution. *Spaceflight mechanics 1999* 265–284 (1999).
28. Kelly, A. C. *et al.*in *Small Satellite Missions for Earth Observation* (Sandau, R., Roeser, H.-P. & Valenzuela, A.) 19–28 (Springer Berlin Heidelberg, 2010).at <http://www.springerlink.com/content/t56u6315274q6554/abstract/>
29. Chichka, D. F. Satellite clusters with constant apparent distribution. *Journal of Guidance, Control, and Dynamics* **24**, (2001).
30. 65 Authors from the Astronautics Community *Space Mission Engineering:The New SMAD*. (Microcosm Press, 2011).